Korean J. Chem. Eng., 35(4), 835-846 (2018)
DOI: 10.1007/s11814-017-0348-y

pISSN: 0256-1115
eISSN: 1975-7220

Optimization design research of air flow distribution in vertical radial flow adsorbers

Yao Li*, Haiqing Si*,†, Bing Wang*, Lu Xue, and Xiaojun Wu*****

*College of Civil Aviation, Nanjing University of Aeronautics and Astronautics, Nanjing 211106, China
**Suzhou Xinglu Air Separation Plant Technology Development Co., Ltd., Suzhou 215000, China
***China Aerodynamics Research and Development Center, Mianyang 621000, China
(*Received 2 June, 2017 • accepted 19 December, 2017*)

Abstract−Non-uniform flow distribution usually exists in a vertical radial flow adsorber, which significantly decreases the utilization of adsorbents. We adopted numerical simulation methods based on the ANSYS Fluent 15.0 software to study the flow pattern in vertical radial flow adsorber, where programs of user-defined functions (UDF) were set up to interpret component equation, momentum equation and energy equation. To solve the problem of non-uniform air distribution, the relationship between the radial pressure drop across the bed and the ratio of cross-sectional area of the central pipe to that of the annular channel was studied, and optimization design of the distributor inserted in the central channel was given by parametric method at the same time. Through comparative analysis in the given experimental condition, the uniformity reached about 99.1% and the breakthrough time extended from 564 s to 1,175 s under the present optimized design method.

Keywords: Flow Distribution, Radial Flow Adsorber, Numerical Simulation, Optimization Design, Distributor

INTRODUCTION

With the rapid development of the steel, metallurgical, chemical and aerospace industries in recent years, the demand for industrial gas such as nitrogen, oxygen has increased sharply [1]. At present, industrial gases are produced mainly by air separation technology, and three common methods for the separation of air components are often used including cryogenic distillation, pressure swing adsorption (PSA) and membrane separation [2]. Cryogenic distillation is related to combining the cryogenic with distillation, which is used to achieve the purpose of gas separation by partial evaporation and condensation continuously with the different boiling point of oxygen and nitrogen. Compared with other separation technologies, cryogenic distillation has high purity and low costs, which is more suitable for mass production of industrial gases [3,19].

However, air is a kind of multi-component mixed gas. Apart from components of oxygen, nitrogen and noble gases, there are other gases in air such as vapor, carbon dioxide, acetylene and other hydro-carbons. Once these impurities enter the cryogenic air separation system, they will precipitate in the low temperature heat exchanger, the turbines and rectification tower, even block the gas distributor and valve on the account of the cooling process of the process air. Under the worse cases, accumulation of acetylene and other hydrocarbon in liquid storage tanks can even cause an explosion [4,17]. Therefore, to reduce the impurity concentration to a prescribed level (carbon dioxide<1 ppm, vapor<0.1 ppm, hydrocarbon is around a few ppb), the feed air must be pre-treated. This process is called air purification and the molecular sieve adsorption is its main process. However, the disadvantage is that it has a high energy consumption, accounting for about 16% of total energy consumption in cryogenic air separation [3].

The pressure drop and regenerative energy consumption of the

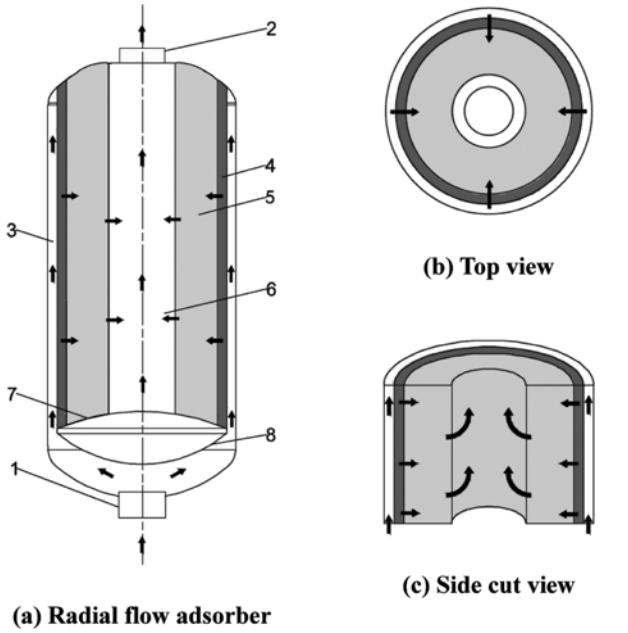

Fig. 1. Schematic of the vertical radial flow adsorber along with top view and side cut view of the radial flow pattern.

1. Inlet	5. Molecular sieve layer
2. Outlet	6. Central channel
3. Annular channel	7. Spherical dish head
4. Alumina layer	8. Deflector

†To whom correspondence should be addressed.
E-mail: sihaiqing@126.com

adsorber bed determine the energy consumption of molecular sieve adsorption system. Compared with traditional vertical axial and horizontal vertical flow adsorbers, the vertical radial flow adsorber has many advantages including small footprint, low bed pressure drop and low regenerative energy consumption. Thus, vertical radial flow adsorbers have been widely used for large-scale cryogenic air separation [3-5].

As shown in Fig. 1, a vertical radial flow adsorber mainly consists of four parts: annular channel, activated alumina layer, molecular sieve layer and central channel [6]. In the adsorption process, air enters the annular channel from the inlet by the air compressor at first, and then it passes through the perforated plate into the alumina layer. After the removal of water vapor, dry air reaches the molecular sieve layer to adsorb carbon dioxide, acetylene and other hydrocarbons. Finally, the process air is collected in the central channel and discharged from the outlet [7]. In this process, due to the unique structure of the radial flow adsorber, non-uniform flow distribution usually exists in a vertical radial flow adsorber, which significantly decreases the utilization of adsorbents and reduces the breakthrough time and even causes safety accidents.

To solve this problem, scholars have done many researches, with many papers focusing on the efficiency of adsorbents, influencing factors, design parameters, and structure optimization. Regarding the efficiency of adsorbents, Yaghoobpour and Li et al. [8,9] studied the mechanism of zeolite molecular sieves, and it was considered to be a very suitable material for adsorbents. Mulgundmath et al. [10] compared the experimental data to the predicted results by extended Langmuir model, and found that it can only be applied as an approximation to predict the experimental binary behavior. Epiepang et al. [11] compared the Tòth, Langmuir-Freundlich (L-F), and the Dubinin-Astakhov (D-A) isotherm models in the low pressure experiment and found the D-A model was the most suitable especially in the low pressure range.

In influencing factors, Kareeri et al. [12] considered that the main factor affecting the uniformity was cross-sectional area of the central pipe and the annular channel. Genkin et al. [13] derived mathematical models of the flow in the radial flow reactor from the energy conservation equation, and found that the gas distribution profile was a function of the central pipe porosity and the ratio of cross-sectional area of the central pipe to that of the annular channel.

As for design parameters, to design the radial bed vessel, Celik et al. [14] proposed a method where the cross-sectional area of the annular channels is in proportion to the mass flow rates of the process gas with the proportionality constant between 0.7 and 1.4. Wang et al. [15] developed a 3D hydrodynamic and mathematical model of a radial flow adsorber, and comparatively studied effects of the cross-section ratio and opening ratio of the central channel and the annular channel. The optimal effect parameter was obtained when the cross-section ratio of the central channel to that of the annular channel reaches 18.9%. With the decrease of the opening ratio of the inner channel within limits, the effect of it in flow uniform distribution becomes more apparent. Wang [16] summarized influences of the breakthrough time and thickness of the adsorbent bed on the adsorption performance. If the total thickness of the adsorbent bed and the air flow rate is constant, the adsorption capacity of the bed is highest where the thickness ratio of the two adsorbents is 0.3.

With regard to structure optimization, Tian et al. [17] proposed a novel radial adsorber by parallel layered beds to better meet requirements of large-scale air separation in terms of achieving good pre-purification performance under the premise of low energy consumption. Rui et al. [18] presented a new parallel connection device to reduce the non-uniformity of flow distribution caused by excessively high bed. Tang et al. [19] proposed a method of inserting a cone in the middle of the center channel to achieve the purpose of uniform pressure drop.

The above studies show that previous analytical and numerical models for studying the flow distribution in a radial flow adsorber are reasonable and practical because of its huge-size and high-cost, and they offer a reference for optimizing the flow adsorber structure and main parameters at the same time. However, there are several weaknesses in the published studies. First, most numerical models omit the deflector and the spherical dish head. Due to such simplifications, these previous modelling methods cannot predict the air flow pattern in the annular channel. Secondly, in the study of structure optimization design, most of these researches ignore the heat transfer and mass transfer in the adsorption process; while the calculation is simplified, it cannot draw the variation of concentration, pressure and temperature of the components in air under these circumstances. Finally, domestic and international researches on the specific structure of distributor are still insufficient. To maximize the utilization of adsorber, adsorbents demand a larger volume ratio, which results in a slender annular channel. When length-diameter ratio of the annular channel is higher, its static pressure is in a decreasing state, which leads to a more complex change in the pressure drop across the bed. Under these circumstances, the traditional conical distributor cannot meet the requirement of uniform pressure drop.

To overcome above limitations, it is necessary to construct a complete model of the adsorber, which greatly improves the accuracy of numerical calculation. Due to the effect of mass transfer and heat transfer on the flow, our major task was to establish a competitive adsorption model of water vapor and carbon dioxide. As far as studies for the specific structure of distributor are concerned, this paper analyzes methods of parametric design, structure of distributors and its process of design. Finally, variations of breakthrough curves with time are obtained, which shows a more accurate description of penetration and provides a more reliable method to optimize the structure of the radial flow adsorbers.

HEAT AND MASS TRANSFER MODELS IN COMPETITIVE ADSORPTION PROCESS

1. Assumptions

To establish mathematical models to simulate H_2O, CO_2 dynamic competitive adsorption process in alumina and 13X zeolite, the following assumptions are required:

(1) Water vapor and carbon dioxide are considered as ideal gases when they are dispersed in the adsorbents;

(2) Adsorption of other gases in the air is ignored, such as nitrogen and a small amount of hydrocarbons;

(3) Particle radius of the alumina and the molecular sieve is the

same;

(4) Adsorption heat is constant and does not vary with temperature;

(5) Linear driving force model is used to express the mass transfer rate;

(6) D-A model is used to describe the adsorption process in the adsorber.

2. Mathematical Models

The control equations of the adsorption process include:

(1) Linear driving force (LDF) model

Mass transfer resistance of molecular sieves is mainly controlled by the large pore diffusion, and the effect of micropore diffusion can be neglected.Therefore, mass transfer rate can be expressed by LDF model:

$$\frac{\partial q_i}{\partial t} = k(q_i^* - q_i) \tag{1}$$

where k is mass transfer coefficient of component; q_i^* is equilibrium absorption capacity of the component i, mol/kg; t is the time.

(2) Adsorption isotherm equation

Compared with Langmuir-Freundlich, Tòth, and the D-A models, the D-A model was found to be best fit especially in the low pressure range.

D-A model contains three parameters: V_0, βF, m.

$$V = V_0 \cdot \exp\left[-\left(C\ln\frac{P_s}{P}\right)^m\right] \tag{2}$$

$$C = \frac{RT}{\beta F} \tag{3}$$

where m represents the distribution of adsorption energies from the adsorbent, the larger the m value, the narrower the micropores, whereas small m value represents adsorbents with wide ranges of pore size; V is volume adsorbed in micropores, cm^3/g; V_0 is a limiting micropore volume, cm^3/g.

(3) Mass conservation equation

$$\frac{\partial(\varepsilon\rho_f Y_i)}{\partial t} + \nabla(\varepsilon\rho_f \vec{u} Y_i) - \nabla(\varepsilon\rho_f D_{i,m}\nabla Y_i) = -S_i \tag{4}$$

$$S_i = M_i\rho_p(1-\varepsilon)\frac{\partial q_i}{\partial t} \tag{5}$$

where ε is bed porosity; ρ_f is gas density, kg/m^3; u is gas velocity, m/s; Y_i is mass fraction of the component i; $D_{i,m}$ is mixed gas diffusion coefficient of the component i, m^2/s; S_i is mass source term of the component i, $kg/(m^3 \cdot s)$; M_i is molar mass of the component i, kg/mol.

(4) Total mass conservation equation

$$\frac{\partial(\varepsilon\rho_f)}{\partial t} + \nabla(\varepsilon\rho_f \vec{u}) = -S_m \tag{6}$$

$$S_m = \sum_{i=1}^{n} S_i \tag{7}$$

(5) Momentum equation

$$\frac{\partial(\rho_f \vec{u})}{\partial t} + (\rho_f \vec{u}\cdot\nabla\vec{u}) = -\nabla p + \nabla(\tau) + \rho_f\vec{g} + \vec{S} \tag{8}$$

where p is the gas pressure, Pa; g is the acceleration of gravity, m/s^2.

However, since the complex structure of adsorption bed and perforated plate cannot be calculated directly, it was often simplified as porous medium and porous-jump model, respectively.

The source term of adsorption bed:

$$\vec{S} = -\left(\mu\frac{\vec{u}}{\alpha} + C_2\rho_f|\vec{u}|\vec{u} + \sum_{i=1}^{n} S_i\vec{u}\right) \tag{9}$$

where C_2 is the inertial resistance factor, m^{-1}; α is the permeability, m^2; The third item is effect of adsorption process on the momentum equation. C_2, α can be calculated by the Ergun equation:

$$\alpha = \frac{d_p^2\varepsilon^3}{150(1-\varepsilon)^2} \tag{10}$$

$$C_2 = \frac{3.5(1-\varepsilon)}{d_p\varepsilon^3} \tag{11}$$

where d_p is diameter of the adsorbent particles, m.

The porous-jump model is a one-dimensional simplified form of the porous media model, and the viscous resistance items can be ignored.

The source term of the perforated plate:

$$\vec{S} = -\left(\frac{1}{2}C_2\rho_f|\vec{u}|\vec{u}\right) \tag{12}$$

where C_2 can be determined according to the empirical formula:

$$C_2 = \frac{1}{C_1^2 dx}\left(\frac{1}{\varphi^2} - 1\right) \tag{13}$$

where dx is the plate thickness, m; φ is porosity of the perforated plate; C_1 is relative to the Reynolds number (Re) and the ratio of plate thickness to hole radius (dx/r). When dx/r>1.6 and Re>4000, C_1 is set to be 0.98 in the paper.

(6) Gas state equation

$$p_i = \frac{\rho_i R_i T}{M_i} = \frac{Y_i\rho_f RT}{M_i} \tag{14}$$

(7) Energy equation

$$\frac{\partial}{\partial t}(\varepsilon\rho_f E_f + (1-\varepsilon)\rho_s E_s) + \nabla(\vec{u}(\rho_f E_f + p)) = \nabla(k_{eff}\nabla T + (\vec{\tau}\vec{u})) + S_f \tag{15}$$

$$S_f = (1-\varepsilon)\rho_s\sum_{i=1}^{n}\left(\Delta H_i\frac{\partial q_i}{\partial t}\right) \tag{16}$$

where E_f is total energy contained in fluid, J/kg; E_s is total energy contained in solid, J/kg; k_{eff} is the effective heat transfer coefficient of bed layer, $W/(m^2 \cdot K)$; τ is stress tensor, $kg/(m \cdot s^2)$; ΔH_i is adsorption heat of gas, J/mol.

(8) Pressure Uniformity

As shown in Fig. 2, the necessary condition for the uniformity of airflow distribution in the adsorber is that the difference between the static pressure p'_B on the torus I and that p'_A on the torus II is equal along the axial height [20].

$$p'_{B0} - p'_{A0} = p'_{B1} - p'_{A1} = p'_{B2} - p'_{A2} = \cdots = p'_{Bi} - p'_{Ai} \tag{17}$$

where

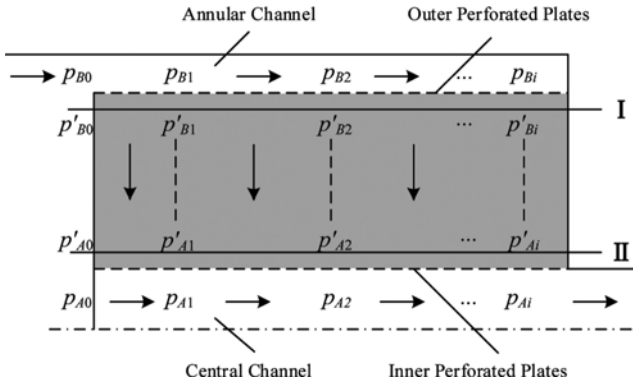

Fig. 2. Schematic diagram of uniform flow distribution in radial flow adsorber.

$$p'_{Bi}=p_{Bi}-\Delta_{Bi} \tag{18}$$

$$p_{Ai}=p'_{Ai}-\Delta_{Ai} \tag{19}$$

where Δ_{Ai} and Δ_{Bi} are perforation resistance of inner perforated plates and that of outer one, respectively.

Substituting Eqs. (18) and (19) into Eq. (17), it is deduced:

$$p_{B0}-p_{A0}-\Delta_{A0}-\Delta_{B0}=p_{B1}-p_{A1}-\Delta_{A1}-\Delta_{B1}=p_{B2}-p_{A2}-\Delta_{A2}-\Delta_{B2} =\cdots=p_{Bi}-p_{Ai}-\Delta_{Ai}-\Delta_{Bi} \tag{20}$$

Since perforation resistance Δ_{Ai} and Δ_{Bi} can be neglected compared to bed pressure drop, airflow uniform conditions can be expressed as follows:

$$p_{B0}-p_{A0}=p_{B1}-p_{A1}=p_{B2}-p_{A2}=\cdots=p_{Bi}-p_{Ai} \tag{21}$$

Thus, the pressure drop across the bed can be substituted by that between two flow channels at the same height, therefore, the uniformity of air distribution can be expressed as follows [21]:

$$U=1-\frac{\sqrt{\frac{1}{N}\sum_{i=1}^{N}(\Delta p_i-\overline{\Delta p})^2}}{\overline{\Delta p}},\quad \overline{\Delta p}=\frac{\sum_{i=1}^{N}\Delta p_i}{N} \tag{22}$$

where U is the uniformity coefficient, N is the the number of data, Δp_i is static pressure difference at i, $\overline{\Delta p}$ is the average of the static pressure difference.

3. Solving Method

We used the finite volume method to discretize the computational domain, and solved control equations of each volume unit by double-precision unsteady implicit solver; the related discrete schemes are shown in Table 1.

The porous media model was used to decrease the computing difficulty. In this process, porous medium model and source term needed to be developed, the correlated parameters of porous medium were set by Eqs. (10) and (11). While the program of Fluent built for single-phase porous media model cannot express the mass transfer and heat transfer process that exists between gas and solid particles in the absorber, programs of user-defined functions (UDF) in Fluent software were set up to interpret the above-mentioned equations, including component equation, momentum equation and energy equation. The two-component D-A equation was applied to define the adsorption equilibrium; LDF model was used to describe the mass transfer process, so the component mass source and the energy source can be defined directly using the macro of DEFINE_SOURCE. Table 2 shows determinations of D-A model parameters.

Table 1. Discrete schemes

Variables	Discrete schemes
Pressure	PRESTO!
Energy	Second order upwind
Momentum	Second order upwind
Component	Second order upwind
Pressure-velocity coupling	Coupled
Density	First order upwind

Table 2. D-A model parameters fit to experimental isotherm data at 293 K[11]

	P_s [atm]	V_0 [m^3/kg]	C	m
H_2O/13X	1.0	3.005E-4	0.125	6.0
CO_2/13X	57.53	3.004E-4	0.120	3.0
H_2O/γ-Al_2O_3	1.0	5.277E-5	0.107	6.0
CO_2/γ-Al_2O_3	57.53	3.153E-5	0.147	2.5

4. Model Validation

Li [7], captured CO_2 from humid flue-gas streams by adsorption method, and conducted penetration experiments to measure the binary adsorption isotherm data of CO_2 and H_2O on zeolite 13X to study the competitive adsorption effect on each other.

The adsorber model was cylindrical with a diameter of 49 mm and a length of 560 mm. The experiment conditions are shown in Table 3, and the physical properties of 13X zeolite are presented in Table 4.

To show the accuracy of the present numerical method, the calculated results were compared with Li's experimental data. Breakthrough time is based on the time point of the sharp increase in CO_2 mole fraction. Numerical results are shown in Fig. 3.

In Fig. 3 the breakthrough time of the test is about 42 s, which demonstrates that the present result can be a satisfactory agreement with the reference one. The reliability and rationality as well as usability of numerical methods were validated by testing results and comparative analyses. Hence, the D-A equation had a greater utility in

Table 3. Experiment conditions

Inlet gas composition [vol%]	Pressure [kPa]	Temperature [°C]	Rate of flow [L/min]
CO_2 10.5; H_2O 3.4; air 86.1	118	30	70

Table 4. Physical properties of 13X zeolite

Property	13X zeolite
Shape	Spherical
Diameter [m]	0.002
Bulk density [kg/m^3]	640.7
Porosity	0.4

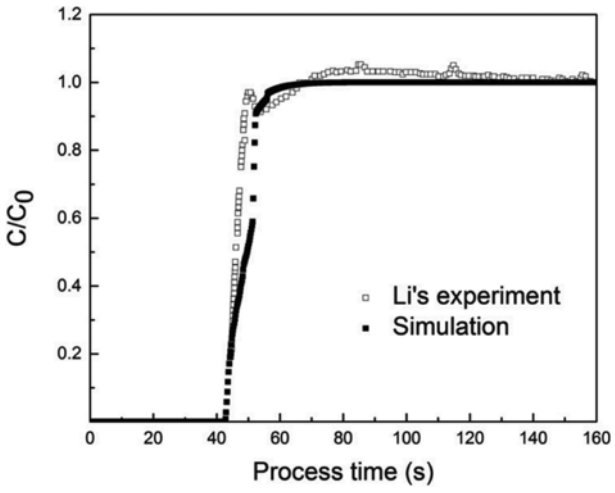

Fig. 3. Comparison of numerical result with experimental one.

describing low-pressure adsorption isotherms.

NUMERICAL INVESTIGATION OF VERTICAL RADIAL FLOW ADSORBER

1. Physical Model

As a result of the limitation of computer hardware, computational cost of the actual model is too large, here a 1 : 5 scale model is considered. As displayed in Fig. 4, inlet and outlet diameter of the adsorber are 200 mm, respectively. Diameter of the central channel is 299 mm. Outer diameter of the molecular sieve bed and the alumina bed is 679 mm and 759 mm, respectively. Diameter of the adsorber is 840 mm. Length of the imperforated plates and structure parameters of the deflector are shown in Fig. 4.

In the present numerical simulation experiments, temperature for the process air and column was set to be 293 K. CO_2 concentration in the inlet was 400 ppm, and flow-rate of the inlet gas stream was 2,000 m^3/h.

2. Grid Sensitivity Analysis

As the model is relatively regular, a professional mesh generation software ICEM-CFD 15.0 was used to generate quadrilateral grid. The grid of radial flow adsorber was shown in Fig. 5, the mesh of the near walls, perforated plates and adsorption area was refined.

The quality of mesh determines the accuracy of calculation. However, due to computer hardware constraints, the grid numbers should not be too large. Fig. 6 displays the static pressure in annular channel as a function of axial height at various grid numbers. Seen from the graph, it has smaller variation of static pressure curves as the number of nodes increases from 30,000 to 120,000. Fig. 7 shows the pressure drop uniformity changes along with the increase of grid numbers. As can be seen, the pressure drop uniformity increases significantly and approaches to a flat after the grid number reaches 30,000, and the error is only around 0.001 when the range of grid number is from 30,000 to 120,000. The accuracy of the mesh was not improved obviously, which indicated that the grid number with 30,000 was enough for the present calculation.

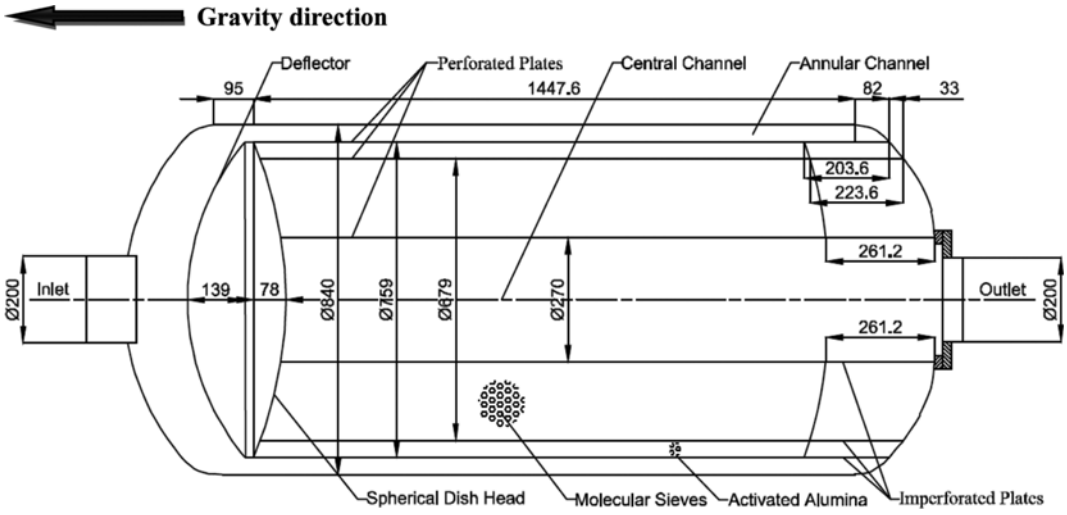

Fig. 4. Label and schematic of the vertical radial flow adsorber.

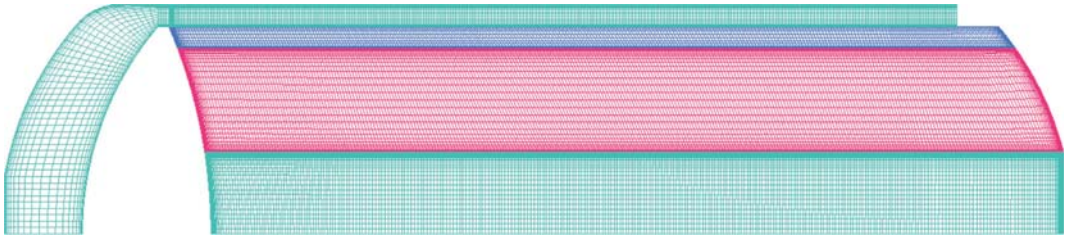

Fig. 5. Mesh of the vertical radial flow adsorber.

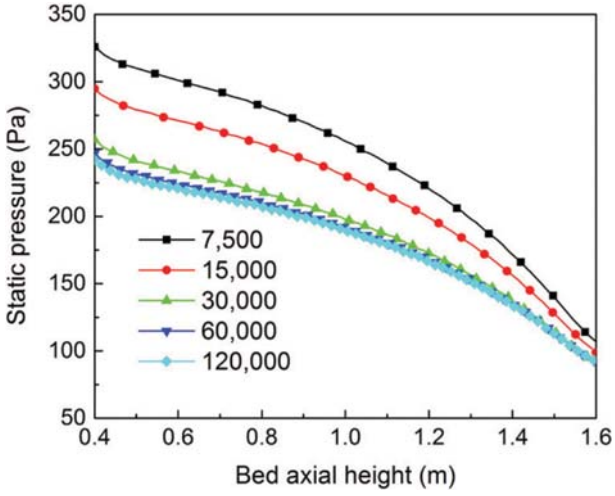

Fig. 6. Changes of static pressure in annular channel along with bed axial height.

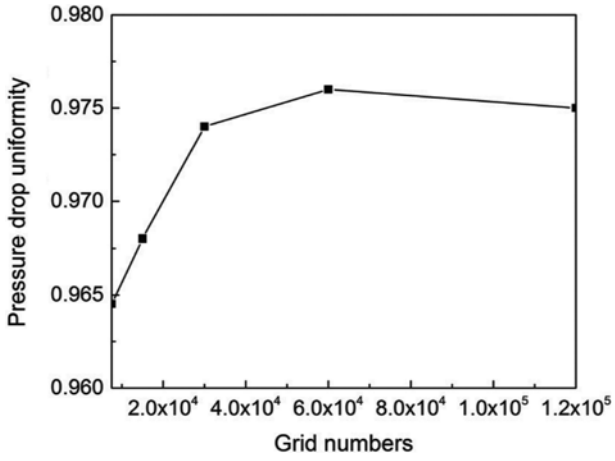

Fig. 7. Changes of pressure drop uniformity along with grid numbers.

3. Boundary Conditions

Using the axisymmetric model, the center line was set as the axis, and inlet and outlet boundary conditions were set as velocity inlet and pressure outlet, respectively. Outer boundary and imperforated plates were set to be a wall, boundary of the alumina and molecular sieve bed was set as boundary conditions of porous jump, adsorbent bed was set as the porous medium. The physical properties of 13X zeolite and γ-Al_2O_3 are listed in Table 5.

Table 5. Physical properties of 13X zeolite and γ-Al_2O_3

Property	γ-Al_2O_3	13X zeolite
Shape of adsorbent	Spherical	Spherical
Diameter[mm]	4	4
Bulk density [kg/m^3]	700	620
Porosity	0.28	0.28
Average pore diameter [nm]	25.2	11.5

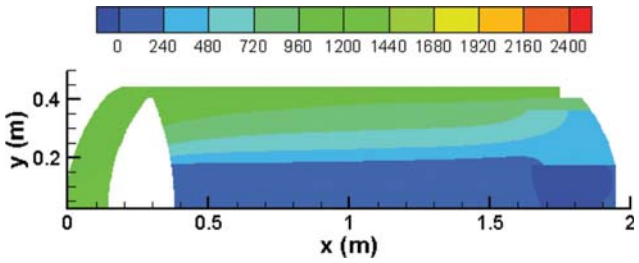

Fig. 8. Static pressure contours of vertical radial flow adsorber.

4. Numerical Method

D-A equation was applied to define the adsorption equilibrium and calculate the saturated adsorption capacity of both adsorbents. A linear driving force model was used to define the mass transfer process. Coupled algorithm of CFD software Fluent was applied to iterate and solve the discrete material equation, momentum equation and energy equation.

NUMERICAL SIMULATIONS AND ANALYSIS

1. Non-uniform Distribution of Air Flow Bed

To simulate the physical model in Fig. 4 using the above method, the air distribution was non-uniform in the adsorption process. As shown in Fig. 8, the main reason for this problem was that radial pressure drop was non-uniform along the adsorbent bed height, which showed that the upper part of the adsorbent had not been effectively used and greatly reduced the utilization of adsorbents.

The non-uniformity can be attributed to the pressure drop between the central pipe and the annular channel. Through the numerical experiment, the gas distribution profile was a function of the ratio of cross-sectional area of the central pipe to that of the annular channel.

2. Influence of Cross-sectional Area on Uniform Flow Distribution

Numerical results are shown in Table 6, and curves of pressure drop vary along the bed axial height, as displayed in Fig. 9. Five groups of numerical tests were carried out to observe effects of cross-sectional area of the central pipe and the annular channel on pressure drop uniformity, which was quantified by Eq. (22).

As can be seen from Fig. 9, when diameter of the central pipe and annular channel is 0.27 m, 0.84 m, respectively, the normalized pressure drop curve is closer to that of uniform flow. Apart from that, the difference between the maximum and the minimum is around 10%, which indicates that the flow distribution is

Table 6. Changes of pressure drop uniformity along with different diameters of the central and annular channel

Group	Diameter of the central channel [m]	Diameter of the annular channel [m]	Pressure drop uniformity [%]
1	0.29	0.84	97.25
2	0.27	0.84	97.38
3	0.25	0.84	96.79
4	0.27	0.82	92.97
5	0.27	0.86	96.88

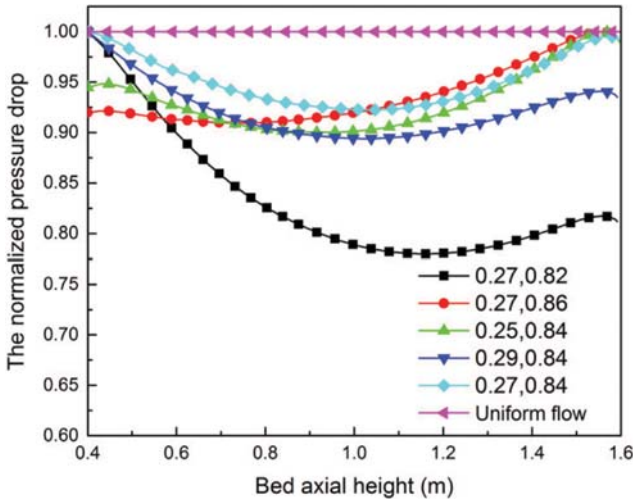

Fig. 9. Changes of normalized pressure drop along with different diameters of the central and annular channel.

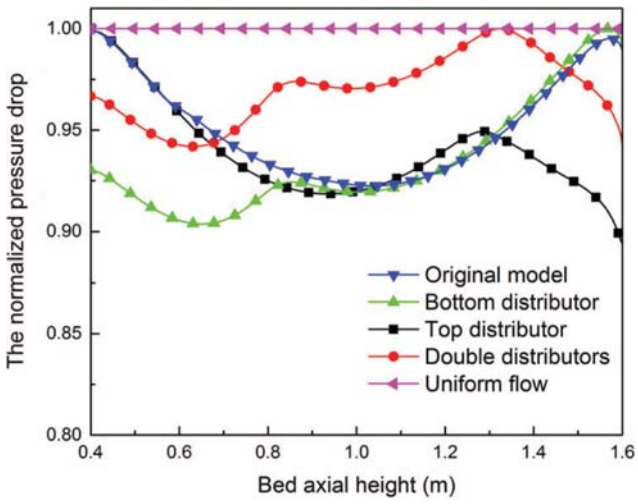

Fig. 11. Changes of normalized pressure drop along with different distributors in the central channel.

still a great potential to develop. Table 6 shows that while the diameter of annular channel is 0.84 m and that of central channel is 0.25 m, 0.27 m, 0.29 m, the pressure drop uniformity is 96.79%, 97.38%, and 97.25%, respectively. However, while diameter of central channel is 0.27 m and that of annular channel is 0.82 m, 0.84 m, 0.86 m, pressure drop uniformity is 92.97%, 97.38%, and 96.88%, respectively. From this point of view, the pressure drop uniformity was influenced by the cross-sectional area of the central pipe slightly, and effects on the cross-sectional area of the annular channel were very significant.

3. Numerical Optimization Study on Distributor

3-1. Influence of Three Kinds of Distributor on Uniform Flow Distribution

Based on the above results and analyses, some new methods are proposed to improve the flow distribution including the insertion of the distributor into the central pipe to change the pressure drop in the inner and outer channel.

To verify the effect of inserting the distributor, three different designs including the position of the distributor at bottom, top and both sides, were studied. Finally, the calculated results from these designs were compared with the original model, as shown in Fig. 10.

From Fig. 11 the overall pressure drop has a slight rise while the pressure drop along the radial direction of distributor shows an extremely steep decrease. According to this characteristic, the design of inserting the upper and lower distributors simultaneously in the both sides of central channel, as shown in Fig. 10(d), is suitable to uniform the pressure drop, which becomes low in the middle but relatively higher on two ends.

3-2. Optimization Method on Uniform Flow Distribution

Before the optimization of the distributor, the actual assembly difficulty and manufacturing costs should be considered first; therefore, we present the following three prerequisites:

(1) While the upper distributor is hollow, the lower distributor is set be a solid to prevent the formation of reflux;

(2) Since the upper distributor is connected to the outlet of the adsorber, the top diameter of the upper distributor is the same size as the diameter of outlet;

(3) Distributors need to be connected with wire mesh or perforated plate (omitted in the calculation) to prevent dust and other solid impurities from being discharged through the outlet. Hence, the bottom diameter of the upper distributor should be consistent with the top diameter of the lower distributor to reduce the fabricating difficulty and cost.

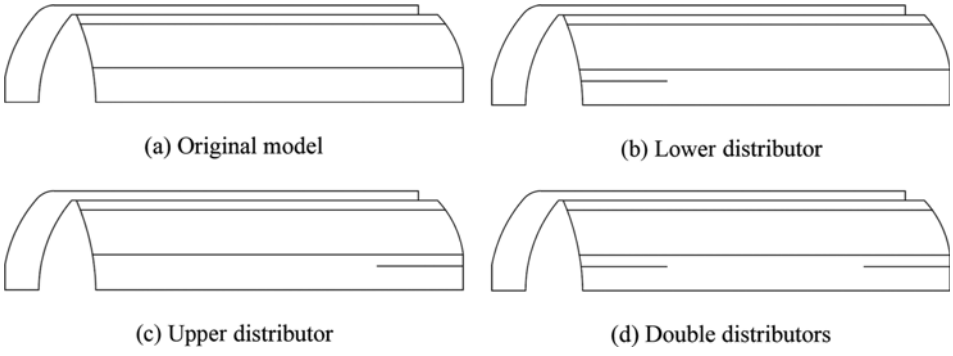

Fig. 10. Four different designs of distributor in the central channel.

Table 7. Changes of pressure drop uniformity along with different lengths of the lower and upper distributor

Diameter of distributors [m]	Length of the lower distributor [m]	Length of the upper distributor [m]	Pressure drop uniformity [%]
0.18	0.38	0.57	98.7236
	0.40	0.57	98.7817
	0.42	0.57	98.7713
	0.40	0.55	98.7669
	0.40	0.59	98.7506
0.20	0.34	0.55	98.8869
	0.36	0.55	98.9171
	0.38	0.55	98.8081
	0.36	0.53	98.8300
	0.36	0.57	98.9167
0.22	0.30	0.50	98.8157
	0.30	0.52	98.8737
	0.30	0.54	98.8238
	0.28	0.52	98.7909
	0.32	0.52	98.8438

Considering the variety of structural parameters, the optimization process is divided into two steps: global optimization and local optimization.

In the global optimization process, distributors are designed as tubes with equal-diameter to study the effect of diameter on the uniformity under the different lengths of distributors. Results are shown in Table 7, diameters of distributors are gradually decreasing from 0.22 m to 0.18 m, and the uniformity of pressure drop can reach the maximum of 98.9171% when the distributor diameter is 0.20 m.

Fig. 12 presents changes of normalized pressure drop along with the different lengths of distributors. Clearly, the following three conclusions can be summarized:

(1) Pressure drop in the bed was reduced at the position where the distributor was inserted, which can be explained as the increase of frictional resistance. Furthermore, while the pressure drop decreased with the length and diameter of distributor, the overall radial pressure drop had a slight rise.

(2) When inserting the lower distributor which was less than 1.0 m, the pressure drop uniformity at the height range from 0.4 m to 1.0 m was changed, but the pressure drop uniformity at 1.0 m to 1.6 m remained constant. Similarly, while the pressure drop

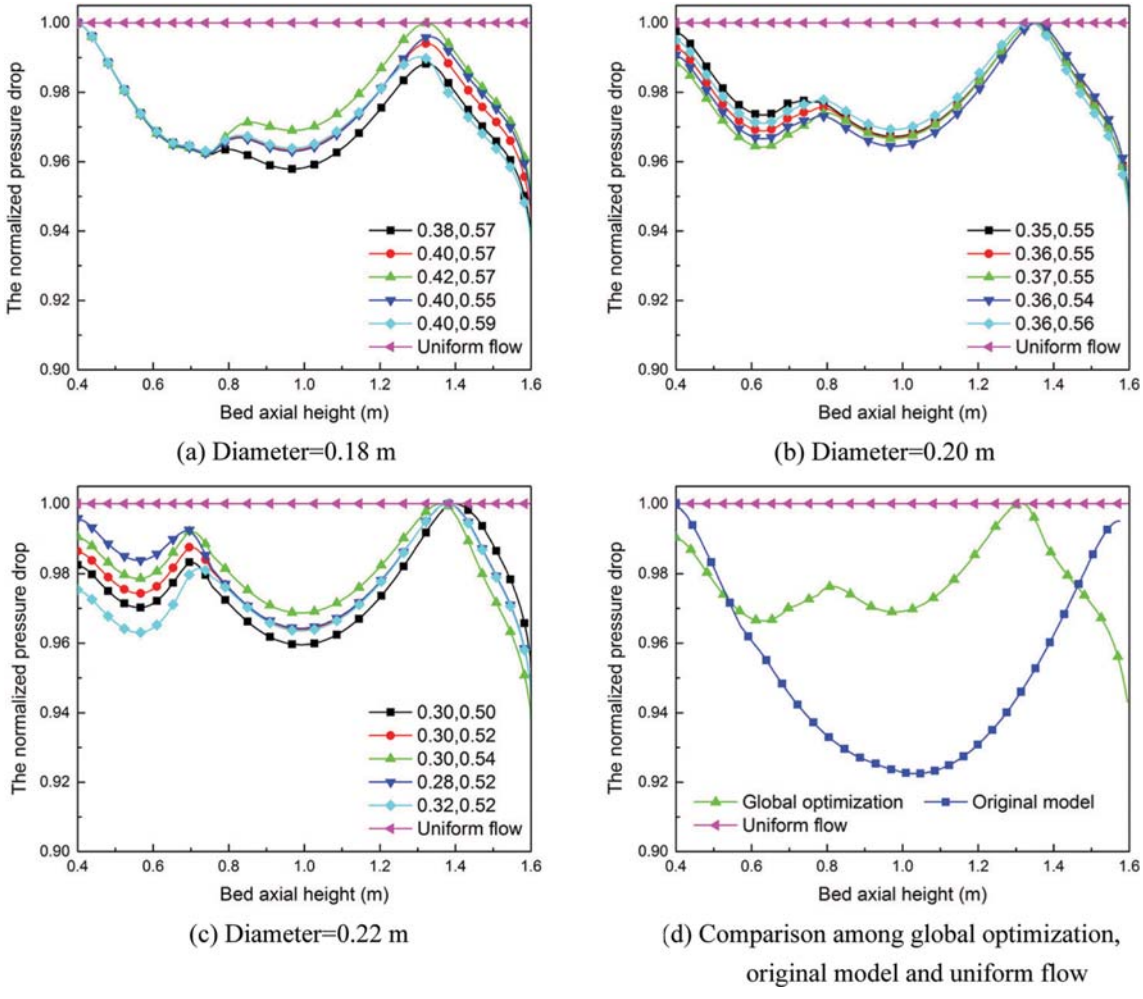

Fig. 12. Changes of normalized pressure drop in global optimization process.

uniformity was changed at the height range from 1.0 m to 1.6 m, it was unchanged at 0.4 m to 1.0 m after inserting the upper distributor.

(3) The distributor could only affect the value of pressure drop in the middle of the central pipe, and not be able to impact its uniformity.

According to the above three conclusions, to conduct the design, the central channel can be divided into two sections to analyze, one is from 0.4 m to 1.0 m and another is from 1.0 m to 1.6 m. If these two sections can achieve the maximum uniformity at the same time, the overall pressure drop will reach the best uniform state. This is called local optimization process.

According to the feature of the optimized curve in Fig. 12(d), where pressure drop in the bed is higher at the height of 0.4 m and lower at 1.6 m, a uniform flow distribution can be achieved by the following two ways: one is to change the length of the upper or lower distributor, and the other is to increase the bottom diameter of the lower distributor or the top diameter of the upper distributor. Here, since the upper pipe is connected to the outlet of the adsorber with a diameter of 0.2 m in this paper, its top diameter needs to be consistent with that of outlet, which shows that the upper distributor can only be designed as a tube with equal-diameter.

To realize the optimal structure, distributor diameter and its length must be considered synthetically in the structure design of the distributor. In the region from 0.4 m to 1.0 m, length and bot-

Table 8. Changes of pressure drop uniformity along with length and bottom diameter of the lower distributor from 0.4 m to 1.0 m

Length of the lower distributor [m]	Bottom diameter of the lower distributor [m]	Pressure drop uniformity [%]
0.37	0.24	99.6625
0.37	0.26	99.6713
0.37	0.28	99.5446
0.36	0.26	99.6228
0.38	0.26	99.5555

Table 9. Changes of pressure drop uniformity along with length of the upper distributor from 1.0 m to 1.6 m

Group	Length of the upper distributor [m]	Pressure drop uniformity [%]
1	0.53	98.6865
2	0.54	98.7032
3	0.55	98.6511

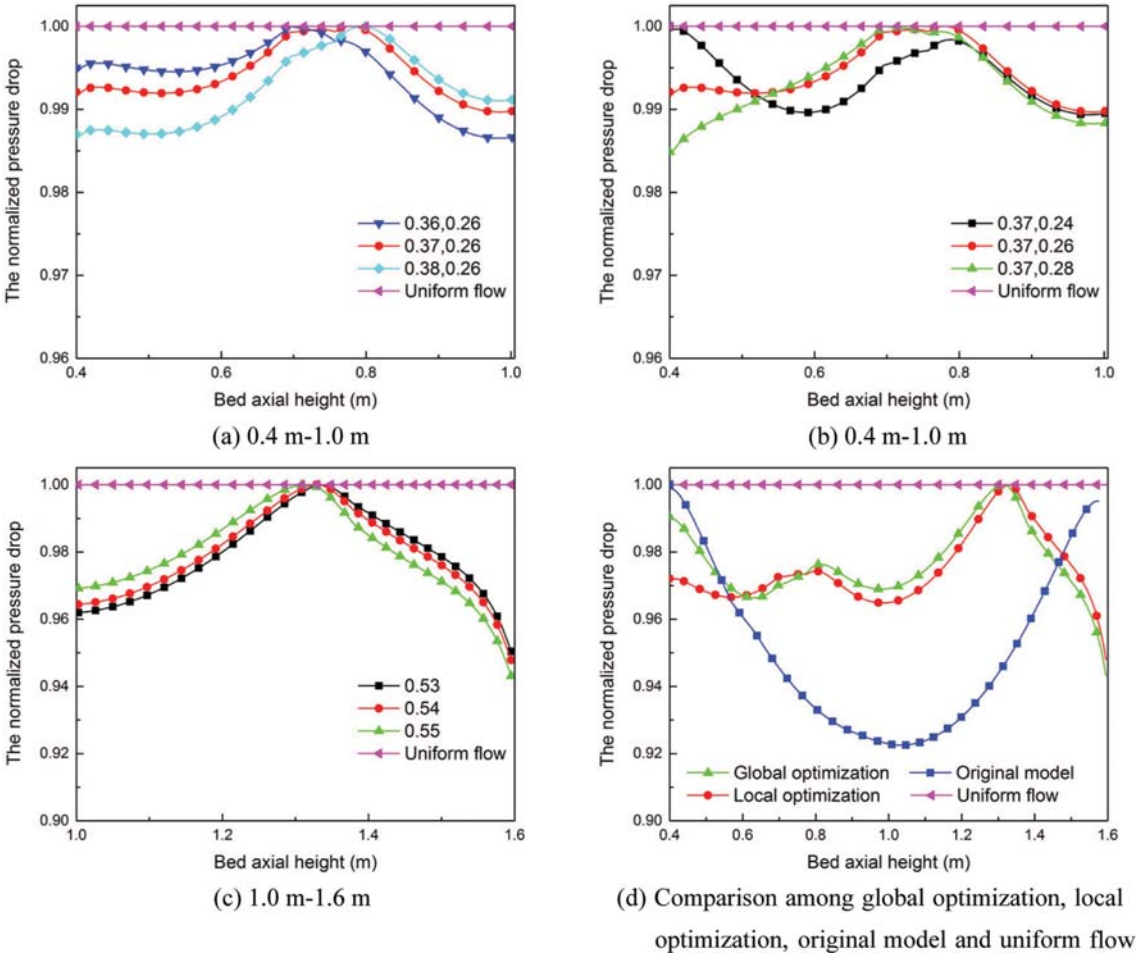

Fig. 13. Changes of normalized pressure drop in local optimization process.

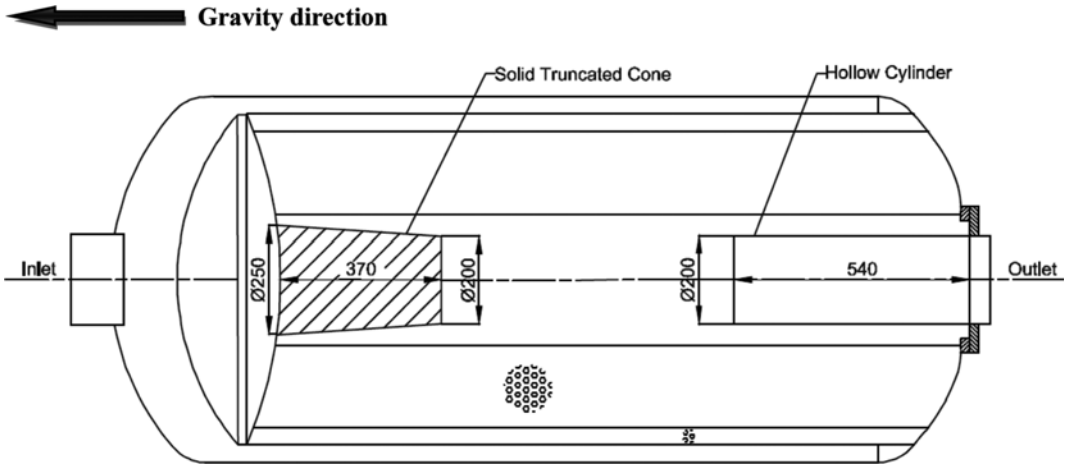

Fig. 14. Label and schematic of the optimized vertical radial flow adsorber.

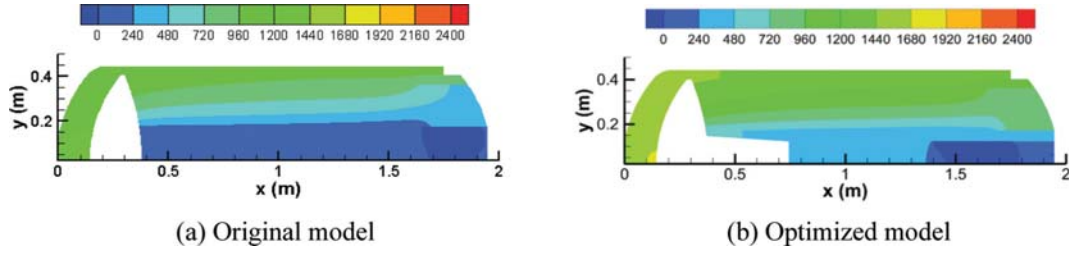

Fig. 15. Comparison of static pressure contours between original model and optimized model in vertical radial flow adsorber.

tom diameter of the lower distributor on pressure drop uniformity is depicted in Table 8. From 1.0 m to 1.6 m, length of the upper distributor on pressure drop uniformity is revealed in Table 9.

Fig. 13(a) and (b) presents the changes of normalized pressure drop along with different length and diameter of lower distributor, respectively. It is indicated from Fig. 13(a), the increase of distributor length can lead the peak of the pressure drop curve to gradually shifting right along the bed axial height; the pressure drop decreases on the left side of the peak point, while the right side one increases. Fig. 13(b) shows that as the bottom diameter of the lower distributor increases, the pressure drop in the bottom area of central channel gradually declines. In addition, when the length and bottom diameter of the lower distributor is 0.37 m and 0.26 m, respectively, the pressure drop on the left and right side of the peak is closer to the symmetrical state, which makes the uniformity of pressure drop eventually reach the maximum of 99.6713% from 0.4 m to 1.0 m. Fig. 13(c) clearly illustrates the relationship between length of the upper distributor and normalized pressure drop when diameter of the upper distributor is 0.20 m. It is revealed by the comparison that the pressure drop is much less affected by upper distributor length than that of lower one. When the length of the upper distributor is 0.54 m, the uniformity of pressure drop can reach the maximum of 98.7032% in the region from 1.0 m to 1.6 m. Fig. 13(d) reveals the comparison of pressure drop among the global, local optimization, original model and uniform flow. Clearly, the pressure drop curve of local optimization is the flattest and its uniformity increase from 97.38% to 99.13%.

3-3. Effect of Different Factors on Flow Field

Based on the above analyses, the pressure drop of the bed has the best uniformity when the lower distributor is a conical frustum with a length of 0.37 m and its top and bottom diameters are 0.2 m and 0.26 m, respectively; the upper distributor is a cylindrical tube with a length of 0.54 m and a diameter is 0.2 m here. The present structure can be shown in Fig. 14, while the upper tube is hollow, the bottom conical frustum is set be a solid to prevent the formation of reflux.

Compared with two contours from Figs. 15(a) and (b), although the overall static pressure of the optimized adsorber increases slightly, the axial and radial static pressure distributions are more uniform in the adsorbent bed.

The adsorber is mainly used to adsorb CO_2 in the air. Under the same amount of feed air, the longer the CO_2 is monitored at outlet, it is adsorbed more completely. On the other hand, the longer the CO_2 penetrates the adsorbent, the adsorber has a more uniform flow field and a better performance. As can be observed in the Fig. 16(a), the penetration time of the optimized model is obviously prolonged, which is caused by more uniform airflow and higher utilization of adsorbents.

Generally, CO_2 reaches adsorption saturation when its concentration is in excess of 1ppm, breakthrough time of the original model and optimized model is 564 s and 1,175 s, respectively, as shown in Fig. 16(b). After calculation, the adsorption amount of CO_2 was 5.59 mol without distributors, and 11.657 mol adsorbed by molecular sieve and alumina when inserting the optimized distributors,

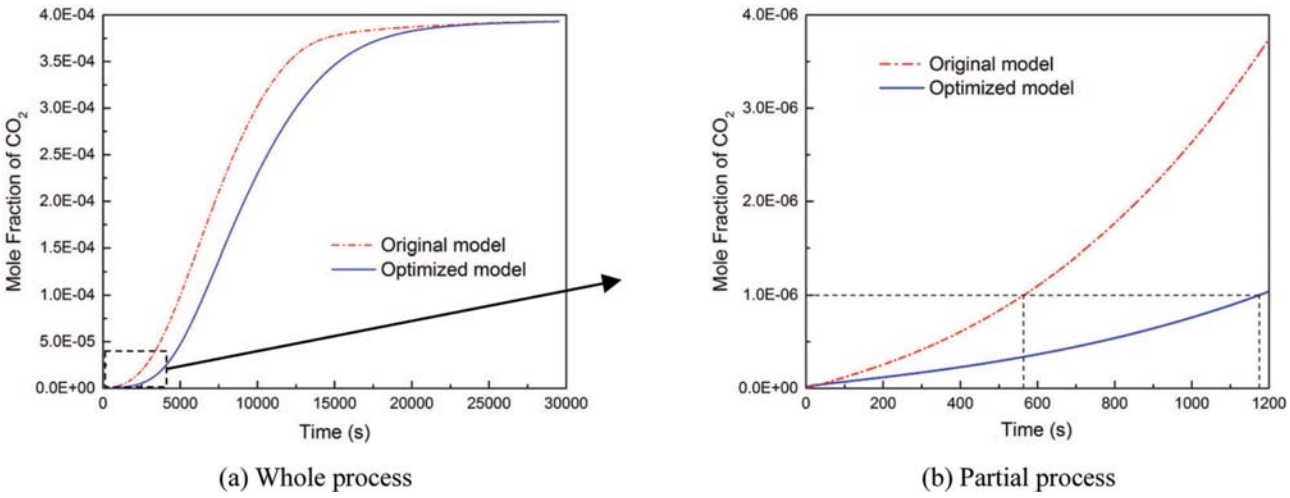

Fig. 16. Comparison of breakthrough curve between original model and optimized model in vertical radial flow adsorber.

and the efficiency was raised by nearly two times in the improved scheme.

CONCLUSIONS

Two-dimensional numerical simulation of the vertical radial flow adsorber was carried out using Fluent commercial software. Changes of the radial pressure drop across the bed along the axial height were obtained, and the design of the optimized distributor was determined by studying the effect on the radial pressure drop. Conclusions are as follows:

(1) It could be more accurately described using mathematical models and numerical tests in this paper with the competitive adsorption of CO_2 and H_2O in the adsorber.

(2) The static pressure in the annular channel of the model was gradually reduced, which belonged to the friction-controlled model. The radial pressure drop along the axial height of the experimental model was low in the middle and high on both sides. When the diameter of cross-sectional area of the central pipe and the annular channel was 0.27 m and 0.84 m, respectively, the adsorber achieved the best performance.

(3) According to effects of the distributor on pressure drop, the ideal structure for the distributor in the central pipe was obtained, which greatly improved the utilization rate of adsorbents.

NOTES

The authors declare no competing financial interest.

ACKNOWLEDGEMENT

The project is funded by the Fundamental Research Funds for the Central Universities with NO: NS2015063.

NOMENCLATURE

C : DA equation parameter
C_2 : inertial resistance factor
D : mixed gas diffusion coefficient [m^2/s]
d_p : diameter of adsorbent particles [m]
E : total energy [J/kg]
F : energy distribution function of adsorbent surface [mol/kJ]
g : acceleration of gravity [m/s^2]
ΔH : adsorption heat [J/mol]
k : mass transfer coefficient
k_{eff} : effective heat transfer coefficient [$w/(m^2 \cdot k)$]
M : molar mass [kg/mol]
m : DA equation parameter
N : number of data
P : partial pressure [Pa]
P_s : saturation pressure [Pa]
p : static pressure [Pa]
Δp : static pressure difference [pa]
$\Delta\overline{p}$: average of static pressure difference [Pa]
q : equilibrium adsorption capacity [mol/kg]
R : gas constant [J/mol/K]
S : mass source term [$kg/(m^3 \cdot s)$]
T : absolute temperature [K]
t : time [s]
U : uniformity degree
V : volume adsorbed in micropores [cm^3/g]
V_0 : limiting micropore volume [cm^3/g]
Y : mass fraction
α : permeability [m^2]
β : DA equation parameter
ε : bed porosity
ρ : density [kg/m^3]
τ : stress tensor [$kg/(m \cdot s^2)$]
u : velocity [m/s]
μ : dynamic viscosity [m^2/s]

Subscripts

i : 1 is water vapor; 2 is carbon dioxide
f : fluid

s : solid

REFERENCES

1. A. Ebrahimi, M. Meratizaman, H. A. Reyhani, O. Pourali and M. Amidpour, *Energy*, **90**, 1298 (2015).
2. M. Mehrpooya, M. Kalhorzadeh and M. Chahartaghi, *J. Clean. Prod.*, **113**, 411 (2016).
3. X. J. Zhang, J. L. Lu, L. M. Qiu, X. B. Zhang and X. L. Wang, *Chinese. J. Chem. Eng.*, **21**, 494 (2013).
4. F. G. Kerry, *Industrial Gas Handbook*, CRC Press, Florida (2006).
5. H. Y. Wang, Y. S. Liu and X. Yang, *Chem. Ind. Eng. Prog.*, **33**, 542 (2014).
6. M. Zhang, *Cryogenic. Technol.*, **2**, 8 (2006).
7. G. Li, P. Xiao, P. A. Webley, J. Zhang and R. Singh, *Energy Procedia*, **1**, 1123 (2009).
8. E. Yaghoobpour, A. Ahmadpour, N. Farhadian and M. Shariaty-Niassar, *Korean J. Chem. Eng.*, **32**, 494 (2015).
9. R. J. Li and Z. B. Zhu, *Chem. React. Eng. Technol.*, **24**, 368 (2008).
10. V. P. Mulgundmath, F. H. Tezel, T. Saatcioglu and T. C. Golden, *Can. J. Chem. Eng.*, **90**, 730 (2012).
11. F. E. Epiepang, J. Li, Y. Liu and R. T. Yang, *Chem. Eng. Sci.*, **147**, 100 (2016).
12. A. A. Kareeri, H. D. Zughbi and H. H. Al-Ali, *Ind. Eng. Chem. Res.*, **45**, 2862 (2006).
13. V. S. Genkin, V. V. Dil-Man and S. P. Sergeev, *Int. Chem. Eng.*, **13**, 24 (1973).
14. C. E. Celik and M. W. Ackley, EU Patent, 2,624,946 (2014).
15. H. Y. Wang, Y. S. Liu and Y. Meng, *Chinese J. Eng.*, **1**, 91 (2015).
16. X. Wang, *Cryogenics*, **1**, 19 (2013).
17. Q. Q. Tian, G. G. He, Z. P. Wang, D. H. Cai and L. P. Chen, *Ind. Eng. Chem. Res.*, **54**, 7502 (2015).
18. D. Z. Rui, X. J. Zhang, Y. Chen and L. M. Qiu, *Chinese J. Chem. Eng.*, **11**, 4485 (2015).
19. Z. L. Tang, M. Y. Xu and J. Zhang, *J. Tianjin Univ.*, **3**, 305 (2016).
20. C. F. Zhang, Z. B. Zhu, M. S. Xu and B. C. Zhu, *J. Chem. Ind. Eng.*, **1**, 67 (1979).
21. R. J. Li, C. X. Cui, Y. Q. Wu and Z. B. Zhu, *Chin. J. Proc. Eng.*, **2**, 209 (2010).